

Chapitre 3

Modélisation numérique de la ventilation naturelle dans une pièce et comparaison aux modèles empiriques

Ce chapitre présente les résultats de différents modèles CFD appliqués à la ventilation naturelle et les compare avec les résultats expérimentaux obtenus au chapitre précédent et les modèles analytiques-empiriques.

Dans la première partie, les équations de base de la simulation CFD, les différents modèles de turbulence, les conditions aux limites ainsi que la méthode de construction du maillage sont présentés.

La deuxième partie compare les résultats obtenus par simulation numérique avec les résultats d'essais réalisés au Chapitre 2. En particulier, le modèle en régime transitoire est appliqué pour comparaison aux essais de gaz traceur en laboratoire et le modèle en régime stationnaire est appliqué pour comparaison aux essais in-situ. Le maillage et le choix des conditions aux limites sont effectués en fonction des configurations de bâtiments et du type de ventilation (mono façade ou traversante). Les courbes de décroissance de concentration de CO_2 , de champ de vitesses et de pressions, ainsi que les profils de turbulence, sont examinés.

La configuration du bâtiment servant aux essais in-situ est particulière puisqu'elle est dotée d'une loggia. Ce cas est, de ce fait, étudié plus en détail au travers d'un article. On y étudie en ventilation traversante l'impact sur le taux de renouvellement d'air de la présence d'une loggia en façade du bâtiment. On s'intéresse aussi à la comparaison des débits d'air obtenus entre les configurations "sous le vent" et "auvent" lorsque la porosité (taux de percement) des façades avant et arrière est fortement différente.

Les simulations CFD permettent de mieux identifier le domaine d'application des modèles analytiques-empiriques.

3.1 Hypothèses, choix de modèles pour la détermination du débit de renouvellement d'air

3.1.1. Equations de Navier-Stokes

La simulation numérique de la ventilation naturelle consiste à résoudre les équations de Navier-Stokes, qui sont des équations aux dérivées partielles. Les équations intègrent dynamiquement la température, la vitesse, la direction, l'humidité, la pression et la viscosité de l'air dans l'espace, et ne peuvent pas être résolues par des méthodes analytiques. À l'aide du développement de la CFD, on peut maintenant obtenir des solutions de ces équations par une discrétisation numérique, sous des hypothèses préétablies.

Les équations représentent la conservation de la masse, le bilan de quantité de mouvement et la conservation de l'énergie dans un domaine fluide. Ces équations considèrent le fluide comme un milieu continu.

- Equation de continuité:

$$\frac{\partial \bar{u}_i}{\partial x_i} = 0 \quad (3.1)$$

- Bilan de la quantité de mouvement :

$$\rho \frac{\partial \bar{u}_i}{\partial t} + \rho \frac{\partial \bar{u}_i \bar{u}_j}{\partial x_j} = -\frac{\partial \bar{p}}{\partial x_i} + \frac{\partial \tau_{jk}}{\partial x_j} + \rho g_j \quad j = 1,2,3$$

$$\tau_{jk} = \mu \left(\frac{\partial u_j}{\partial x_k} + \frac{\partial u_k}{\partial x_j} \right) + \frac{2}{3} \frac{\partial u_l}{\partial x_l} \delta_{jk} \quad j = 1,2,3 \quad (3.2)$$

- Bilan d'énergie:

$$\rho C_V \frac{\partial \bar{T}}{\partial t} + \rho C_P \frac{\partial \bar{u}_i \bar{T}}{\partial x_i} = -\left(\lambda + \frac{C_P \mu_t}{Pr_t} \right) \frac{\partial^2 \bar{T}}{\partial x_i^2} + \dot{q} \quad (3.3)$$

Où u_j est le j-ième composant du vecteur vitesse, p est la pression statique, ρ est la masse volumique, τ_{jk} est le tenseur des contraintes visqueuses, μ est la viscosité dynamique, δ_{jk} est égal à 1 si $j = k$, zéro autrement, g_j est le j-ième composant du vecteur de force de gravité, C_V et C_P sont les capacités thermiques massiques à volume et à pression constante respectivement, considérées indépendantes de la température, T est la température absolue, λ est le coefficient de conductivité thermique, aussi considérée indépendante de la température, et \dot{q} représente une éventuelle source de chaleur.

Les méthodes de calcul pour résoudre les équations 3.1 à 3.3 sont bien développées, même pour un écoulement tridimensionnel en fonction du temps. Pourtant, il n'y a pas de modèle de calcul pouvant être appliqué à des problèmes pratiques généralement turbulents. Cela tient au fait que la capacité informatique nécessaire pour la méthode DNS (Direct Numerical Simulation) dépasse de loin ce qui

est généralement disponible, même si elle a été améliorée de plusieurs ordres de grandeur aujourd'hui.

Pourtant, les écoulements turbulents sont courants. Pour y répondre, des modèles de turbulence ont été développés. Ces méthodes consistent à simplifier la turbulence aux petites échelles en appliquant des moyennes spatiales (LES - Large Eddy Simulation) ou temporelles (RANS - Reynolds Averaged NS) aux équations de Navier Stokes.

La méthode RANS consiste en une représentation statistique des champs de vitesse décomposant la vitesse en une valeur moyenne¹ et une fluctuation par rapport à cette moyenne. On applique cette décomposition dans les équations de la dynamique des fluides ce qui fait apparaître un terme supplémentaire ayant la forme d'un tenseur symétrique (6 composantes à déterminer). On se retrouve ainsi avec plus d'inconnues que d'équations. Pour fermer le système, il est nécessaire d'introduire d'autres équations. On utilise alors des modèles de fermeture tels que les modèles k- ϵ .

3.1.2. Choix des conditions aux limites

La construction du maillage et le choix du domaine de calcul sont des points clés pour le calcul numérique. La compatibilité du maillage à la problématique visée n'est pas seulement une question liée à la résolution de chaque maille, mais aussi à l'architecture du maillage et aux conditions aux limites.

Dans le cas de la ventilation, le domaine de calcul peut être limité à l'espace ventilé associé à des conditions aux limites aux ouvertures mais il est courant d'intégrer aussi l'environnement où le(s) bâtiment(s) situe(nt). La géométrie de chaque élément est toujours simple ou facile à simplifier à base de cubes, de carrés, de ronds, etc. Il est préférable d'utiliser un maillage structuré dans tout le domaine de calcul.

Le choix du domaine va dépendre de la connaissance des conditions limites. La Figure 3-1 illustre l'application en espace intérieur seul. La périphérie du domaine de calcul correspond à l'enveloppe de l'espace ventilé. Les entrées et les sorties doivent alors être spécifiées en tant que conditions aux limites. La Figure 3-1-a correspond à la configuration de la pièce ventilée mécaniquement ayant servi aux essais du Chapitre 2.2. Le débit d'air contrôlé par un ventilateur sert de condition à l'entrée et on spécifie une «pression libre» à la sortie. L'utilisation d'un domaine limité à l'espace intérieur est ici adaptée.

¹ Il s'agit d'une moyenne d'ensemble que l'on peut en pratique calculer pour un processus stationnaire comme une moyenne temporelle.

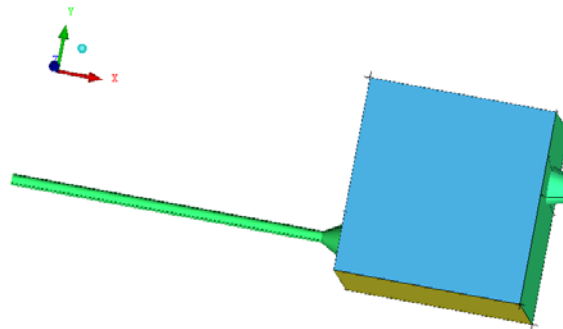


Figure 3-1. choix du domaine : calcul dans l'espace intérieur seulement

Dans le cas de la ventilation naturelle, le modèle est complexe car l'écoulement d'air à travers les ouvertures est lié à la fois au vent et au tirage thermique entre l'intérieur et l'extérieur.

En ventilation naturelle traversante où l'effet du vent est dominant, il est possible d'utiliser le seul espace intérieur comme domaine de calcul.

Toutefois, pour une ouverture libre, il est préférable d'imposer à l'entrée une condition de pression que de vitesse. Ceci suppose de connaître la distribution de pression sur les façades. Pour cela, on peut utiliser des coefficients de décharge prédéterminés en laboratoire. Malheureusement, ces coefficients ne sont pas toujours disponibles (exemple des essais in situ à Cargèse sur un bâtiment avec loggia du Chapitre 2.4).

Il est aussi supposé que l'écoulement intérieur n'a pas d'impact important sur l'écoulement extérieur. En effet, pour un bâtiment avec de très grandes ouvertures, la distribution de pression sur les façades changera quand la fenêtre sera ouverte et le coefficient de décharge ne sera plus identique à celui mesuré dans les conditions du laboratoire. Ceci limite l'application du modèle à des bâtiments à porosité faible ou moyenne.

En ventilation naturelle mono-façade, il paraît difficile de définir des conditions limites à l'ouverture. Une modélisation intégrant des domaines extérieurs est donc indispensable.

L'amélioration de la puissance de calcul des ordinateurs rend aujourd'hui possible d'utiliser un modèle représentant le champ complet. La Figure 3-2 présente le domaine de calcul intérieur + extérieur retenu pour simuler le bâtiment de Cargèse. Avec un tel domaine, l'interaction entre l'intérieur et l'environnement est prise en compte. La simulation est plus réaliste car le profil de vitesse à l'ouverture est généré par le champ de pression.

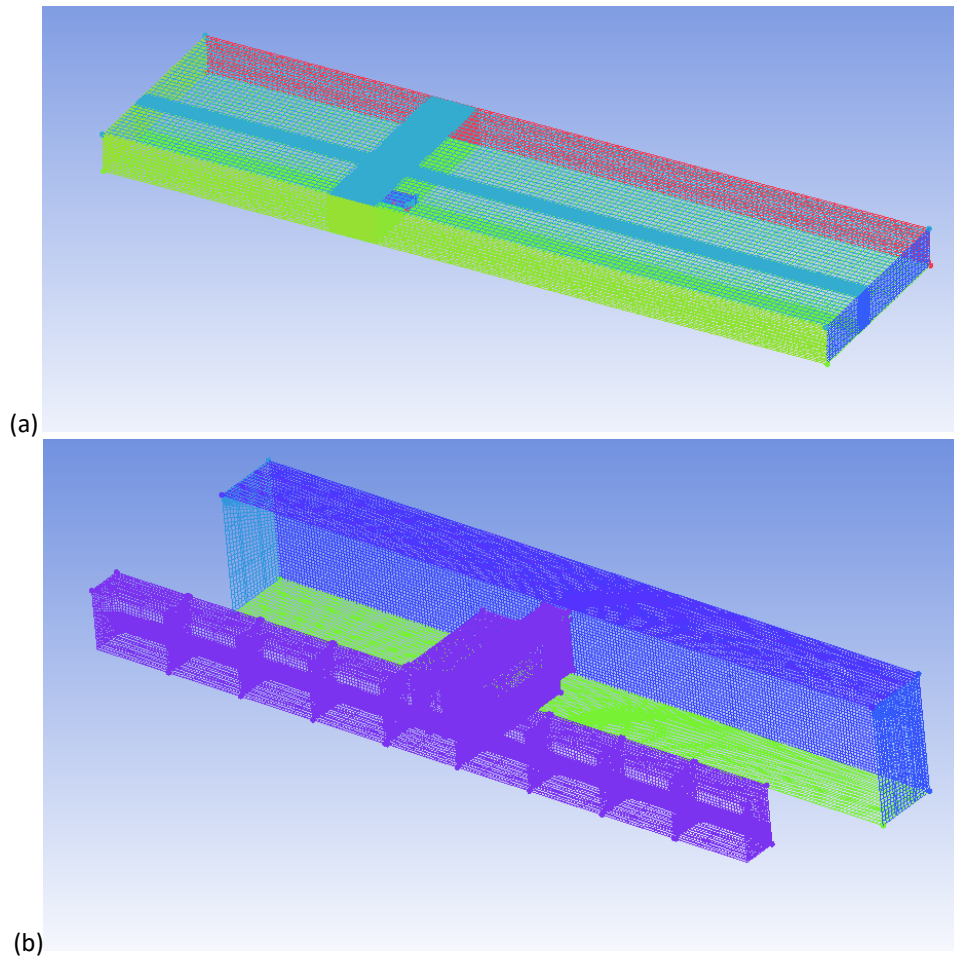


Figure 3-2. choix du domaine géométrique modélisé : calcul en champ complet. a) ensemble du domaine, b) zoom à proximité de la zone intérieure étudiée

Si l'on veut répondre à la question de la qualité de l'air intérieur ou évaluer le taux de renouvellement d'air à travers la fenêtre, le maillage dans le bâtiment doit être assez fin. Au contraire, le domaine extérieur qui sert à générer le champ de vitesse doit être assez large. Ainsi, il est préférable d'utiliser deux maillages de finesse différente puis de les coupler. Un maillage typique en ventilation naturelle est de l'ordre d'un million de mailles.

Les conditions aux limites en champ complet sont plus compliquées que si l'on se limite à l'espace intérieur. Prenons le même exemple, la logique de mise en place de domaine de calcul est donnée ci-dessous

- Le terrain est considéré comme une paroi rugueuse, avec une hauteur de rugosité de 0,15 m;
- L'enveloppe du bâtiment et les parois internes sont modélisées comme des murs lisses;
- La bordure supérieure du domaine est en condition de cisaillement constant;
- Les bordures côtés gauche et droit sont considérées soit comme symétriques, soit comme entrée ou sortie selon la condition du vent;
- L'entrée est considérée comme Entrée de Vitesse;
- La sortie est considérée comme Sortie de Pression.

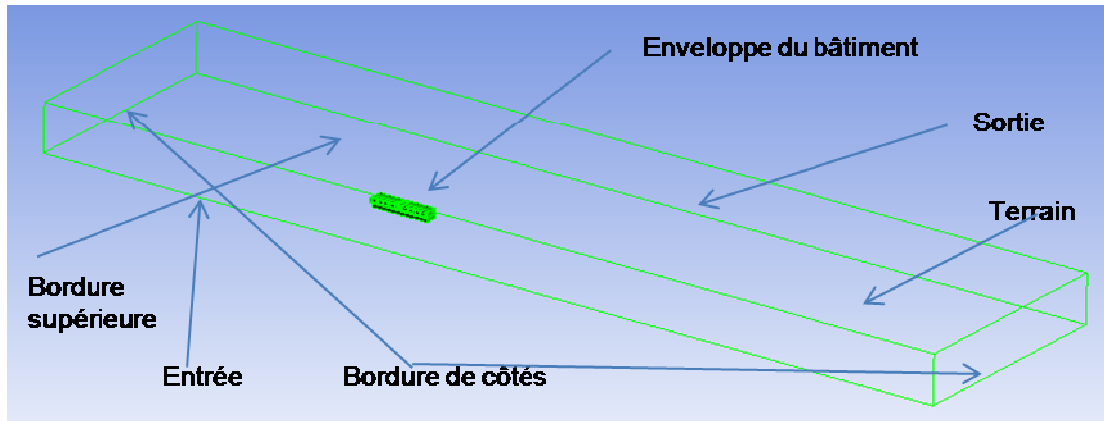


Figure 3-3. choix de condition aux limites

Les détails géométriques sont présentés au Chapitre 3.3.

3.1.3. Détermination du débit de renouvellement d'air

Deux méthodes peuvent être utilisées pour obtenir le taux de renouvellement d'air. La première consiste à intégrer les vitesses dans le plan des ouvertures. Cette méthode est pratique pour la simulation en ventilation naturelle traversante où le sens de l'écoulement au niveau des ouvertures est assez bien établi. Cependant, cette méthode n'arrive pas à bien prendre en compte les éventuelles recirculations d'air dans le plan d'ouverture. L'autre méthode repose sur la simulation de l'émission d'un gaz traceur fictif et le tracé de la courbe de décroissance de sa concentration, comme dans les essais expérimentaux par gaz traceur. Cette méthode est particulièrement adaptée pour la ventilation naturelle mono-façade ou dans le cas d'écoulements fortement perturbés au niveau des ouvertures avec de fortes recirculations.

Les deux méthodes sont employées au chapitre 3.2 en utilisant le modèle en champ intérieur pour le cas de la ventilation mécanique.

3.2 Modélisation de la chambre d'essais ayant servi à établir la méthode par gaz traceur

La chambre de test, longue de 3m, haute de 2m et large de 3m (figure 3-4) est construite avec une entrée d'aspiration et une sortie d'évacuation. Dans les essais, l'entrée est connectée à un conduit d'air dans lequel l'air est insufflé par un ventilateur centrifuge. Des mesures du débit par sondes de Pitot sont utilisées pour mesurer le débit d'air et contrôler le ventilateur. Elles sont installées dans le conduit à 1.5 m de l'entrée de la chambre d'essais. Le conduit en amont est de longueur 5m pour avoir un écoulement pleinement développé. Les débits plats (valeurs correspondantes à la mesure au Chapitre 2.2) sont utilisés comme conditions aux limites à l'entrée du modèle en amont de la chambre d'essais ventilée.

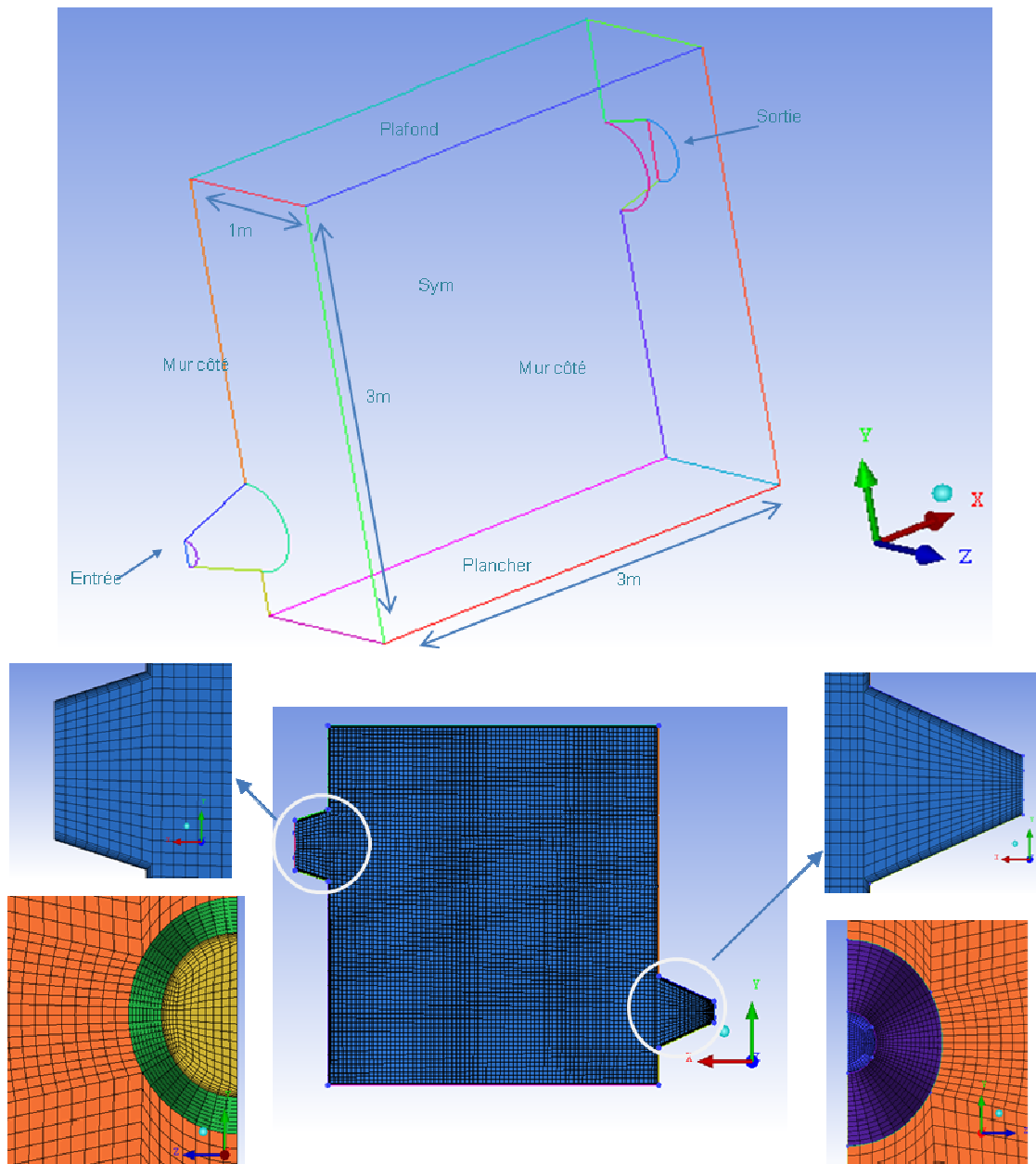


Figure 3-4. Géométrie et maillage du domaine simulé

La Figure 3-4 présente la géométrie et le maillage structuré de la chambre de test. Le maillage a été créé sous ANSYS ICEM avec un «Minimum Orthogonal Quality» de 0.29 et un «Maximum Aspect Ratio» de 54.2. Les conditions aux limites et la taille des mailles sont indiquées dans Tableau 3-1.

Tableau 3-1. Conditions aux limites et taille des mailles pour la simulation CFD

Zone	Conditions aux Limites	Taille des Mailles
Nozzle-In	Wall	2cm
Plancher	Wall	4 cm
Entrée	Velocity-inlet	1 cm
Fluide	Interior	4 cm
Sortie	Outflow	1 cm
Façade	Wall	4 cm
Mur côté	Wall	4 cm
Nozzle-out	Wall	2 cm
Sym	Symmetry	4 cm

Les résultats en simulation de gaz traceur sont donnés sur la figure 3.5.

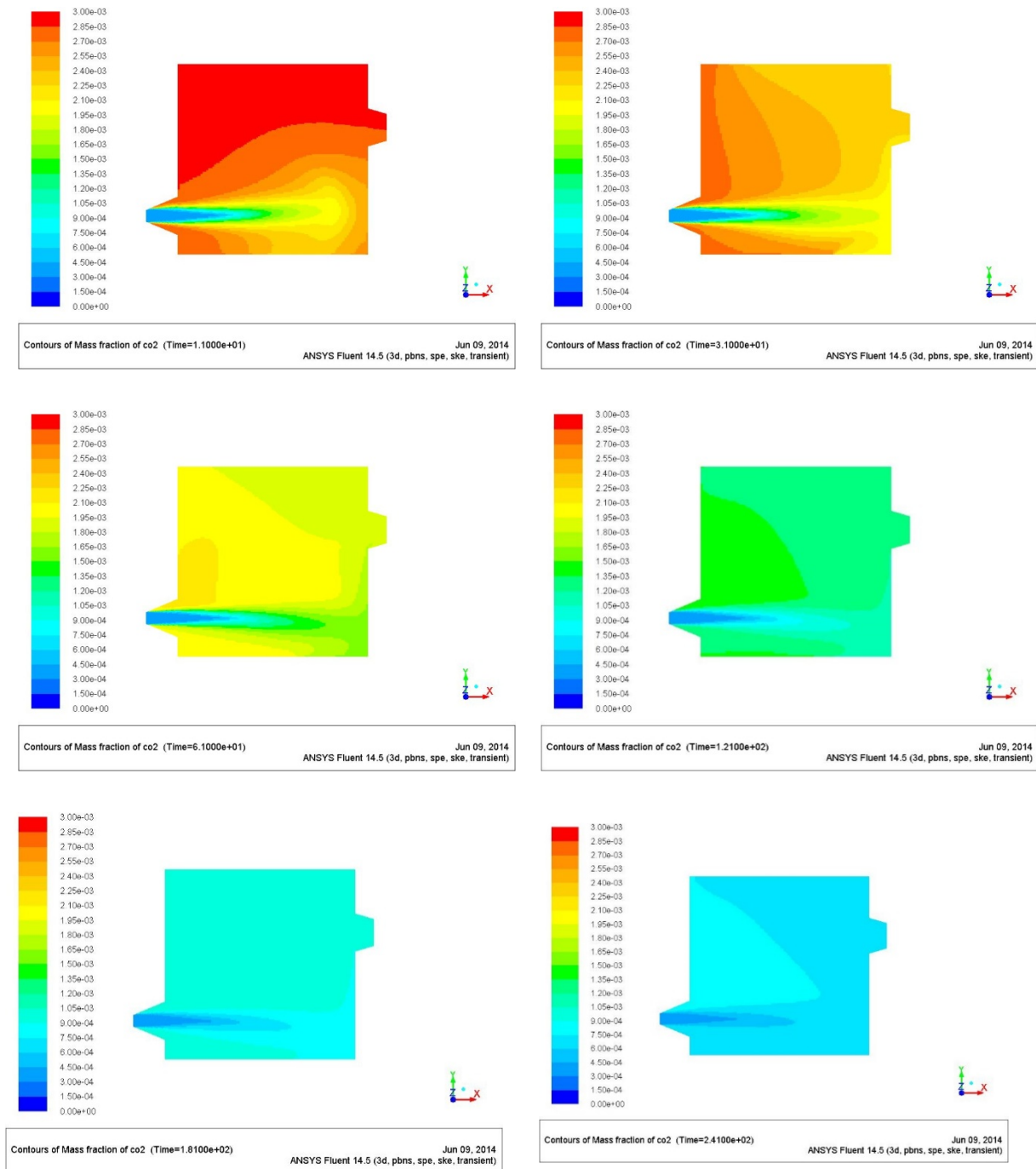


Figure 3-5. Profils de concentration en CO₂ dans la chambre d'essais

La Figure 3-5 montre les profils de fraction massique de CO₂ à différent pas de temps (10s, 30s, 60s, 2min, 3min, 4min respectivement). Le taux de renouvellement d'air de référence de cette simulation est de 32 vol/h. Comme on peut le voir sur cette figure, la décroissance de concentration de CO₂ commence à l'entrée de la chambre et se propage vers le coin en bas à droite, puis vers le coin en haut à droite, puis à gauche, et finalement vers le centre. Un jet d'air se forme effectivement pour ce débit. En fonction du temps, on observe la concentration de CO₂ aux différents emplacements de la chambre d'essais.

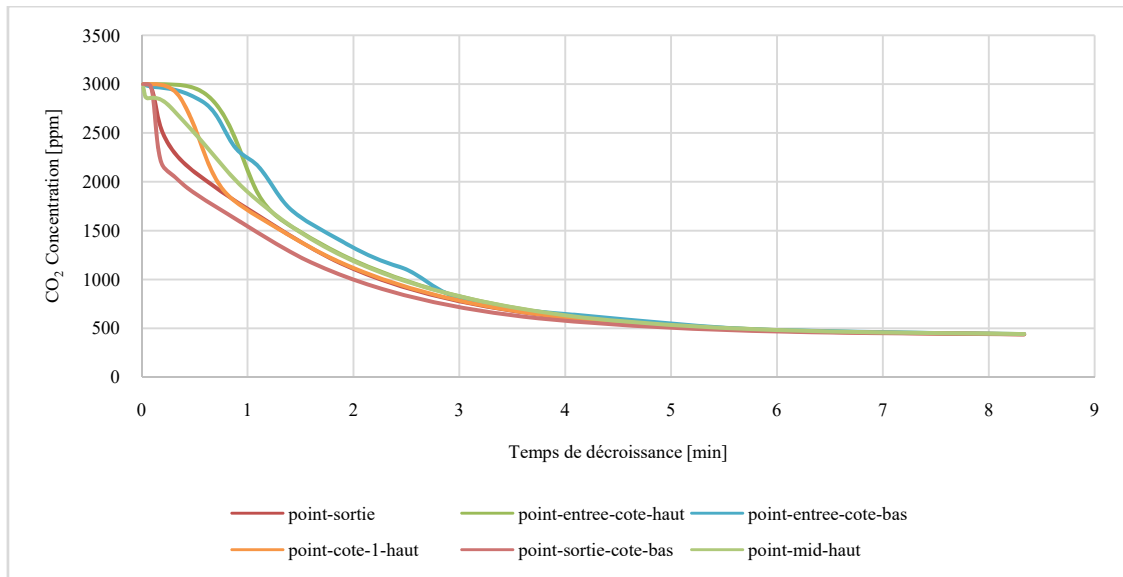


Figure 3-6. Courbe de décroissance en différents endroits de la pièce

Les courbes de décroissance en différents points situés à l’intérieur de la chambre d’essais sont montrées dans la Figure 3-6 à titre d’exemple. Aux premiers instants, une importante déviation est observée due aux mouvements d’air. Les différentes courbes tendent à converger ensuite. Les taux de renouvellement d’air déduits des courbes de décroissance en différents points et pour différents taux de renouvellement d’air sont présentés dans le Tab. 3-2. Le calcul de décroissance porte sur la plage située entre 3000 ppm et 500 ppm.

Tableau 3-2. Synthèse des résultats pour différents taux de renouvellement d’air

ACH_{ref}	ACH_s	$ACH_{g-moyen}$	$Diff_{gr}$	ACH_{g-max}	ACH_{g-min}	Ecart type de l’ ACH_g
vol/h	vol/h	vol/h		vol/h	vol/h	
7.6	7.6	6.8	-13%	8.8	5.2	15%
16.1	16.1	14.8	-8%	16.8	12.5	12%
24.0	24.0	23.5	-2%	24.7	19.4	6%
32.0	32.0	31.0	-4%	33.4	27.7	6%
40.3	40.3	37.7	-7%	39.7	35.6	7%

ACH_{ref} est le taux de renouvellement d’air de référence; la vitesse du vent correspondante à cette valeur est imposée à l’entrée comme la condition aux limites. ACH_s est le résultat obtenu par l’intégration de vitesse de l’écoulement d’air à la sortie dans la simulation et ACH_g par la méthode du gaz traceur fictif. ACH_{g-m} est le résultat moyen de l’ ACH_g en plusieurs points dans la pièce ventilée. Les résultats sont obtenus pour toutes les valeurs de référence de taux de renouvellement d’air qui apparaissent dans les essais au Chapitre 2.2.

Quand le débit d’air de référence est de 24 vol/h, la simulation obtient un taux de renouvellement d’air moyenné plus proche de la valeur imposée à l’entrée. Pour le débit d’air plus faible ou plus grand, les différences sont plus importantes. D’ailleurs, pour les débits d’air plus importants, l’erreur relative entre chaque point est plus faible. En effet, le choix de la plage de calcul dans la méthode du

gaz traceur fictif a une influence clé sur les résultats obtenus. Il existe une recirculation à l'intérieur de la pièce et les résultats de simulation moyennés entre plusieurs points s'accordent mieux avec les valeurs de référence. En général, une différence entre la méthode du gaz traceur fictif et l'intégration des vitesses est d'environ 10%, ce qui est de l'ordre de grandeur de la différence observée entre chaque point de mesure. Toutefois, la méthode du gaz traceur fictif représente un temps de calcul beaucoup plus lourd car chaque pas de temps demande des calculs itératifs pour tracer la courbe de décroissance. Seule la méthode de l'intégration des vitesses sur le plan de l'ouverture est employée au chapitre 3.3 en utilisant le modèle en champ complet pour la configuration de bâtiment à Cargèse.

3.3 Influence de la présence d'une loggia dans la ventilation traversante

Revue scientifique publié dans « Building and Environment », accepté

Numerical simulation of wind-driven natural ventilation: effects of loggia and facade porosity on air change rate

Shuqing CUI*, Pascal STABAT, Dominique MARCHIO

MINES ParisTech, PSL Research University, CES - Centre d'efficacité énergétique des systèmes, 60 Bd St Michel 75006 Paris, France

*Corresponding email: shuqing.cui@mines-paristech.fr

Keywords: cross-ventilation, loggia effect, Computational fluid dynamics (CFD), Experimental validation, correlation, parametric analysis

Abstract

Building envelope geometry has an important impact on cross-ventilation performance. Presence of external architectural structures (e.g. a loggia), and opening surfaces can all affect ventilation performances. All these factors lead to deviation in the wind-driven ventilation rates predicted by semi-empirical models (correlations). Thus, this study is focused on the effects of a loggia and window opening size on cross-flow ventilation rates estimated by Computational Fluid Dynamics (CFD). CFD has been validated on field measurements in a low-rise building, with a steady-state Reynolds-Averaged Navier-Stokes (RANS) model. Ventilation performance is evaluated for buildings with or without a loggia with different opening sizes and various wind conditions. We find the presence of the loggia reduces the average air change rate by 27%, except for one wind direction at which a vortex is formed in the loggia and directs the airflow into the opening. However, the empirical models based on the orifice equation fail to precisely predict the ventilation rate for large windward-side windows. Large windows should be installed on the façade exposed to the prevailing wind, so as to enhance ventilation performance.

Introduction

Natural ventilation is an efficient strategy to reduce building energy consumption and improve occupant satisfaction and indoor air quality [Allard, 1998]. Natural ventilation is driven by wind- and/or buoyancy-induced pressure differences [Hunt and Linden, 1999][Li and Delsante, 2001][Larsen and Heiselberg, 2008]. Due to its complex mechanism, ventilation performance prediction remains a primary concern [Kato et al. 1992][Mistriotis et al. 1997][Straw et al. 2000][Mochida et al. 2006][Wright and Hargreaves, 2006][Hu et al. 2008][Stavarakakis et al. 2008][Norton et al. 2010][Nikas et al. 2010] and how to integrate it into the heating, ventilation, and air conditioning (HVAC) control system of a building is a hot topic [Wang and Greenberg, 2015][Hiyama et al. 2015].

Among Building Energy Simulation tools, a common approach is to use natural ventilation correlations derived from semi-empirical models. Semi-empirical ventilation models, usually based on orifice equation and Bernoulli's principle, are simple ways to involve the turbulence effect in to

calculation of air change rate or air change per hour (ACH). The two types of ventilation, single-sided ventilation and cross-ventilation, are often treated separately [Evola and Popov, 2006][Caciolo et al., 2012]. On one hand, when conventional empirical models are used to deal with single-sided ventilation, the main difficulties are the entering and leaving air circulations at the same opening and the interaction between wind and buoyancy effects. Caciolo et al. combined experimental study and numerical parametric analysis to figure out a correlation that involves the main turbulence effects [Caciolo et al. 2013]. On the other hand, the mechanism of cross-ventilation is relatively simple because the major driving force is the wind effect, and therefore, the form of cross-ventilation correlations is usually simple. According to dimensionless analysis [Etheridge, 2002], the ventilation rate can be expressed only as a function of the wind direction and Reynolds number. When the environmental surroundings, building geometry and wind conditions are known, the developed correlations can be used to easily assess the ventilation rate. However, these correlations are not applicable to all building configurations.

Building envelope features greatly affect the air flow patterns. In particular, the position, size and shape of openings can significantly alter the air flow within a building. A very large opening size may change the pressure coefficient on the building envelope and thus probably the airflow near the building [Etheridge, 2012]. This would make the real ventilation rate and theoretical prediction considerably different, especially in wind-driven cross-ventilation. As reported, when the facade porosity (window surface ratio on the facade) exceeds a threshold (in this case ranging from 10% to 33%), the correlation method underestimates ACH [Serfert et al. 2006].

Different opening shapes can greatly change the natural ventilation performance [Shetabivash, 2015][Wang et al. 2015], so appropriate selection of opening features is a major objective in the pre-design phase of building construction. Today, Computational Fluid Dynamics (CFD) is generally applied to obtain more precise predictions of ventilation performance [Chen, 2009]. In complex building configurations mentioned above, conventional correlation methods are unable to assess the ACH correctly. Field measurements are impractical in the pre-design phase. Nevertheless, the low-cost numerical models help researchers to investigate flow patterns and pressure distribution and acquire additional information that is basically inaccessible from experiments.

CFD has already been used to study various building envelope configurations. Kobayashi et al. used experimental and numerical methods to investigate how flow patterns and pressure distributions are affected by the opening size in cross-ventilation [Kobayashi et al. 2010]. When the opening size exceeds a certain value (15% of the facade's surface), the windward-side vortex disappears and consequently the flow resistance in the ventilated space is reduced. In a building with a semi-enclosed individual balcony, the flow pattern changes strongly with the local flow diversion and recirculation on the facade compared to the configuration without a balcony [Montazeri and Blocken, 2013]. The general deviation is 10%, but the discrepancy in each room is not systematic. Moreover, the presence of a porous second-skin facade could decelerate the local wind speed by reducing pressure gradients across the facade spacing [Montazeri et al. 2013]. These two studies focus on the wind comfort of the occupants in a high-rise building and nearby pedestrians. Ai and Mak investigated the pollutant dispersion between rooms in a high-rise building with semi-enclosed balconies [Ai and Mak, 2014]. Shetabivash performed numerical simulations on a multi-cell building with several window shapes and positions [Shetabivash, 2015].

However, none of these studies have dealt with a configuration with loggia. A loggia hereafter is referred to an architectural feature which is a wholly-covered exterior space from the ground to the upper level, as opposed to a semi-enclosed balcony. Such a building element will significantly change the pressure distribution on a building envelope and the ventilation rates in the rooms.

In addition, building configurations are not always symmetrical in reality. When the window surfaces on the two opposite walls are not equal, neither the envelope pressure distributions nor the indoor flow patterns are the same. However, changes in natural ventilation rate according to the wind direction (from the opposite facade instead of the front facade) have not been predicted by the correlation methods and are barely studied previously.

The major objective of this study is to investigate the effects of loggia and facade porosities on the cross-ventilation performance. ACH is chosen as a principal indicator of natural ventilation performance to be systematically analyzed.

Field Tests

Building Environment

The study target is a single-cell room in a low-rise building on the seaside in Corsica, France (Fig.1). This building is located in a typical Mediterranean climate with hot dry summers. The instant wind speeds and directions were measured by an ultrasonic 3D anemometer installed on the roof (10 m high). The front wall is oriented east-southeast facing the sea. The surrounding buildings on the seaside are all located much lower and thus hardly form any obstacle to the wind. On the back side of the building, the facade is quite embedded in the hill located behind the building. The building is a two-floor hotel with 9 identical rooms on each floor. Each room has a separated loggia structure on its seaside facade that is surrounded on four sides by a floor, two vertical walls and roof. The building is designed to promote cross-ventilation through two openings of different sizes on opposite walls. There is a large window (1.08 m^2) on the front wall and a small window (0.35 m^2) on the back wall. Both windows can be opened completely for cross-ventilation. The porosities of the front and back walls are 11.1% and 3.6%, respectively. The ventilated space is 18 m^2 with a volume of 48 m^3 . The room size is $3.6 \times 2.7 \times 8.2 \text{ m}^3$ (length \times height \times width) including 1.6 m of the loggia. This building configuration is the reference geometry in the following study.



Figure 1. Building environment.

Measurement Instrumentation

The ventilation rate was measured with the tracer gas technique based on the concentration decay method. The measurement method and decay curve calculation were already assessed in preliminary laboratory tests and field tests [Cui et al. 2014][Cui et al. 2015]. Thus, only the basic principles are presented here.

The tracer gas used for the tests was carbon dioxide, which is inert, colorless, odorless, nontoxic below 5000 ppm and slightly heavier than air ($= 1.87 \text{ kg/m}^3$ at $15 \text{ }^\circ\text{C}$ and ambient pressure). Carbon dioxide can be mixed properly with the wind from a ceiling fan.

Before each test, CO_2 was injected into the room for a few minutes at a flow rate adjusted by an auto-valve. The injection was stopped when the indoor concentration reached about 4000 ppm. The fan went on working for a few minutes after the end of the injection, until the concentrations measured at 9 positions in the ventilated space (Fig.2) were the same, which indicates the uniformity of CO_2 concentration. Owing to the presence of CO_2 in the air, the outdoor background concentration (C_{bg}) was simultaneously measured to compensate for the possible external variation. Then the fan was stopped and the windows were opened to measure the decay of CO_2 concentration. If the ventilation rates are maintained constant, the decay curve is strictly exponential. The measures on the decrease of instantaneous concentration determine the volumetric flow rate (q) and ACH of fresh air.

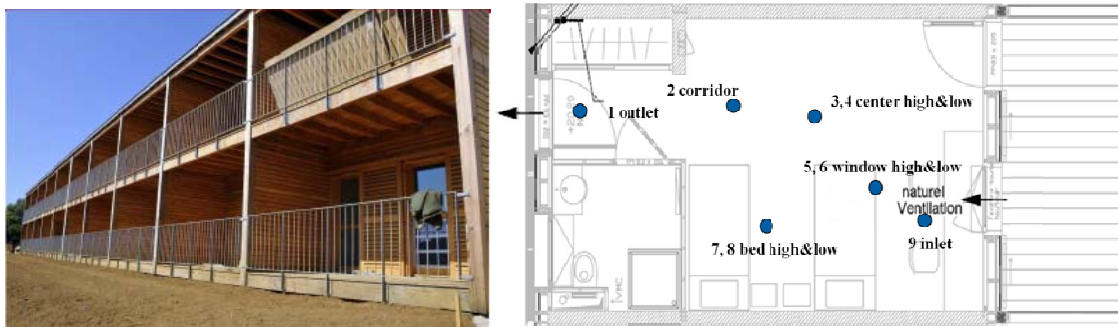


Figure 2. Building configuration facade view and gas tracer tests implantation schema.

CO_2 concentrations were measured every 15 seconds. The volumetric flow rate q can be calculated from any two points on the decay curve as follows:

$$q = \frac{1}{\Delta t} \ln \frac{(C_0 - C_{bg})}{(C_f - C_{bg})} \quad (1)$$

where C_0 is the initial concentration and C_f is the final concentration.

The q is divided by the room volume to determine ACH:

$$ACH = \frac{q}{V} \quad (2)$$

Least-square regression is carried out between $C_0=3000$ ppm and $C_f=600$ ppm to determine the ACH measured at each position. The difference between each position represents the indoor air mixing degree.

Experimental Results and Comparison to Correlation Methods

The measured ACHs are synthesized in Table 1 with the averaged wind speed and wind direction for each test. The average uncertainty in each test is 10%. The uncertainty is compounded from three independent error resources by calculating the normalized root-mean-square deviation: uncertainty of sampling and instruments, fluctuation of wind speed and direction in natural ventilation, and non-homogeneous CO₂ concentration during decay. The average values are used to validate the CFD models.

The results of the correlation methods are also listed in Table 1. An analytical expression can be derived from the orifice equation [Etheridge and Sandberg, 1996]. ACH is expressed as the product of effective opening surface A_{eff} , discharge coefficient C_d , wind velocity v_{ref} , and the pressure coefficient ΔC_p (C_p is pressure difference between front and back walls):

$$q = C_d \cdot A_{eff} \cdot v_{ref} \cdot \sqrt{\Delta C_p} \quad (3)$$

The dimensionless ΔC_p is a function of wind direction alone when the building configuration and surrounding environment are known. However, Eq.(3) does not distinguish between the windward and leeward sides of a building with different opening sizes on its opposite facades, which means the predicted ventilation rates under two wind conditions are identical. ΔC_p is usually calculated with empirical or semi-empirical methods [EN 15242, 2007]. Swami and Chandra (SC) correlation [Swami and Chandra, 1987] allows to estimate the C_p change according to the wind incident angle [Orme and Leksmono, 2002]. Despite some improvements to SC correlation recently [Sawachi et al. 2006][Sharag-Eldin, 2007], the original equation is quite commonly applied and implanted in building energy simulation platforms [Crawley et al. 2008]. Therefore, its original form is used as a reference here:

$$C_p = C_p(0^\circ) \cdot \ln \left(1.248 - 0.703 \sin \frac{\theta}{2} - 1.175 \sin^2 \theta + 0.131 \sin^3(2\theta \ln S) + 0.769 \cos \frac{\theta}{2} \right) + 0.071 (\ln S)^2 \sin^2 \frac{\theta}{2} + 0.717 \cos^2 \frac{\theta}{2} \quad (4)$$

where S is the aspect ratio of the building geometry; θ is the wind incident angle.

The results calculated by Rousseau and Mathews (RM) correlation [Rousseau and Mathews, 1996] are listed as well because this correlation is based on field measurements in a low-rise rectangular architecture with a plate roof, which is similar to our configuration. RM correlation is expressed as follows: for $\theta \leq 90^\circ$ and $\theta \geq 270^\circ$

$$C_p = 0.5994 - 0.1426|\sin\theta| - 0.8055|\sin\theta|^2 + 2.0149|\sin\theta|^3 - 2.1972|\sin\theta|^4 \quad (5a)$$

and for $90^\circ < \theta < 270^\circ$

$$C_p = -0.333 - 0.1544|\sin\theta| - 0.1128|\sin\theta|^2 \quad (5b)$$

As showed in Table 1, the SC and RM correlations overestimate the natural ventilation rate by 66.7% and 31.9% on average, respectively. In these calculations, C_d is always considered to be 0.61, which is common for small opening surfaces. However, the correlations that assume homogeneous pressure distribution over the building facades can add uncertainty to calculations [Cóstola et al. 2009]. Since

the correlations provide a shielding coefficient only for far obstacles rather than for shelter structures over the facade, in the present study the main influence factor on the reduction of ventilation performance could be the existence of the loggia.

Table 1. Ventilation rate calculated by correlations compared to field tests

Cases	Wind speed(m/s)	Wind direction(°)	ACHexp (vol/h)	SC Correlation (vol/h)	Deviation	RM Correlation (vol/h)	Deviation
T1	0.63	-158.2	8.2±0.6	9.0	9.7%	5.2	-36.7%
T2	1.98	43.9	10.4±1.5	27.1	160.6%	22.0	111.3%
T3	2.32	22.7	19.0±1.7	32.9	73.1%	30.0	58.1%
T4	2.90	29.3	28.7±2.8	40.6	41.5%	33.9	18.0%
T5	2.12	-52.5	19.3±2.3	28.7	48.5%	21.0	8.6%

CFD Model of the Test Room and Validation

Domain Size and Meshing

CFD simulations should take into account the interactions between outdoor and indoor air flows. This purpose can be achieved by coupled and decoupled approaches. The coupled or ‘whole field’ approach simulates the building and environment simultaneously in the same mesh, thus resolving the above interaction. On the contrary, the decoupled approach treats indoor and outdoor environments separately. Outdoor simulation or field measurements are used as boundary conditions for indoor airflow simulations. These two approaches can be selected for different purposes. For instance, Montazeri and Blocken studied how the presence of a balcony affects the wind speed around the building [Montazeri and Blocken, 2013], so the simulation was only based on outdoor meshing. In the present study which was focused on the indoor air change rate, a coupled method was applied to determine a whole field calculation.

The simulated two-floor building was described in section 2.1. Its size is $32.4 \times 5.4 \times 8.2 \text{m}^3$ (the loggia included in length). The third room from the left on the first floor was used for the experimental campaign and simulated by CFD.

In order to simulate the real wind field around the building, we built a large computational domain of $421.2 \times 32.4 \times 85.8 \text{m}^3$ (13, 6, and 13 times of the building’s length, height, width, respectively). The mesh domain is larger in the leeward zone. The computational field mesh was selected with consideration into wind direction (Fig. 3).

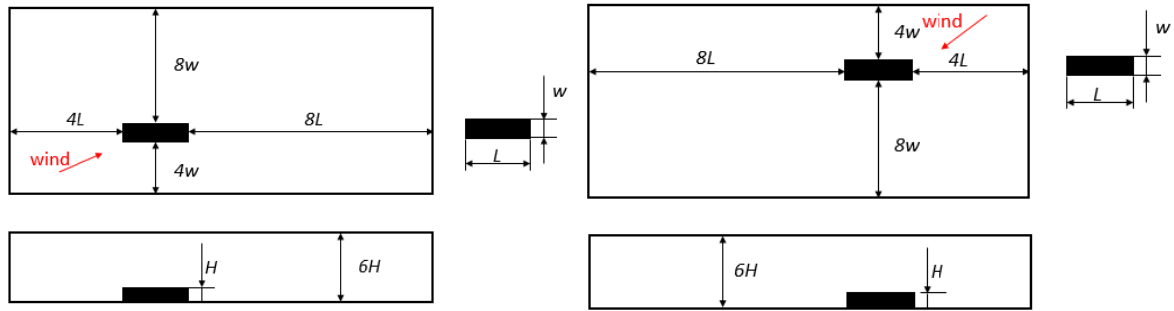


Figure 3. Whole field grid: wind arrives at the front wall (left) or back wall(right).

The sizing and mesh numbers are presented in Table 2. In order to optimize the meshing number, we drew the field domain on a coarse mesh and the ventilated space on a fine mesh. The resulting mesh is constructed in Ansys ICEM [ANSYS, 2014].

Table 2. Mesh size and number

	Reference Grid
Cells	1,888,776
faces	5,752,990
nodes	1,974,554
Minimum orthogonal quality	0.909
Maximum aspect ratio	55

A grid convergence test was performed on three sizes to check the independence of the chosen grid: a coarse grid with 903 744 cells, a normal grid with 1 888 776 cells and a fine grid with 5 066 992 cells. The normal one composed of about 1 million cells for both field and room domains are selected.

The grid was refined in the vicinity of the ground surface, the walls and the openings, with a minimum grid size of 1.5 cm for the room facade, 15 cm for the walls attached to the ventilated room, and 35 cm for other surfaces of the building.

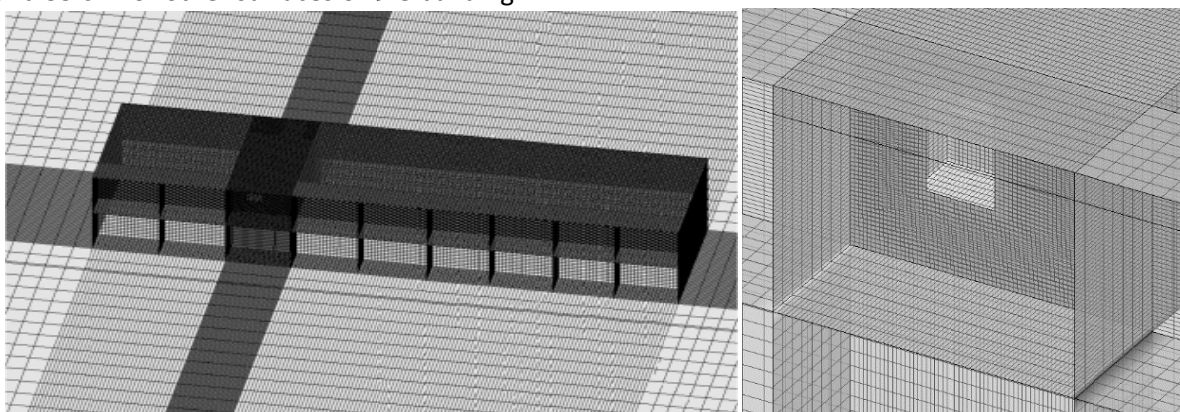


Figure 4. Details of computational domain (left) and building scale (right) on loggia scale.

Boundary Conditions

The boundary conditions are set as follows:

- (1) ground surface: rough wall with a roughness height, z_0 , of 0.15m;
- (2) exterior and interior building walls: no-slip walls;

- (3) top border of the domain: a constant shear stress condition;
- (4) left and right walls: symmetric boundary conditions or no-slip walls;
- (5) inlet boundary: velocity with a logarithmic law;
- (6) outlet boundary: pressure out.

Solver Settings

It is confirmed that the Reynolds-Averaged Navier-Stokes (RANS) model provides acceptable results in most situations with inaccuracy of only 20% and short computation time about 1/30 that of Large Eddy Simulation(LES)[Caciolo et al. 2013]. Here the steady 3D RANS equations were solved on the commercial CFD platform Ansys Fluent 14 [ANSYS, 2011]. The governing RANS equations are written as follows:

$$\frac{\partial \bar{u}_k}{\partial x_k} = 0 \quad (6)$$

$$\frac{\partial}{\partial x_k} (\rho \bar{u}_k \bar{u}_j) = -\frac{\partial \bar{p}}{\partial x_j} + \mu \frac{\partial^2 \bar{u}_j}{\partial x_k^2} - \frac{\partial}{\partial x_k} (\rho \overline{u'_j u'_k}) + \rho \beta (\bar{T} - T_0) g_j, \quad j = 1, 2, 3 \quad (7)$$

$$\frac{\partial}{\partial x_k} (\rho \bar{u}_k \bar{T}) = -\left(\frac{\lambda}{C_p} + \frac{\mu_t}{Pr_t}\right) \frac{\partial^2 \bar{T}}{\partial x_k^2} + \frac{\dot{q}}{C_p} \quad (8)$$

where the overbar indicates ‘time-averaged’. The term involving the Reynolds stresses can be calculated from several turbulence models such as Re-Normalisation Group (RNG) k-ε model and Reynold Stress Model (RSM). Both models were applied to the field test data to compare the prediction accuracy of ventilation performance. The pressure was interpolated by a “PRESTO!” scheme, and pressure-velocity coupling was finished by the SIMPLE algorithm. Second-order upwind discretization schemes were used for both the convection terms and diffusion terms of the governing equations. We assumed convergence when all the scaled residuals leveled off and minimized to 10^{-5} for velocity terms, 10^{-3} for k, ε, continuity and Reynolds stress tensor in RSM. In addition, the mass and energy balances at the opening were checked through surface integration of mass flow and energy.

Calculation of ACH

The simplest way to calculate the ACH from the simulated velocity field is to integrate the time-averaged normal velocity over the opening areas as follows:

$$q = q_{in} = q_{out} = \frac{1}{2} \sum_c^{N_{cells, opening}} \left| \bar{v}_c \cdot \bar{n}_c \right| \cdot A_c \quad (9)$$

where \bar{v}_c is the velocity vector, \bar{n}_c is the unitary vector normal to the opening and A_c is the area of cell c that belongs to the opening. ACH is then calculated from Eq. (2).

This method is straightforward and pertinent in the present case of wind-driven cross-ventilation in a single room where the buoyancy effect can be neglected compared to single-sided ventilation [Allocca et al. 2013][Yang et al. 2006].

Comparison of the CFD Model with Field Measurement

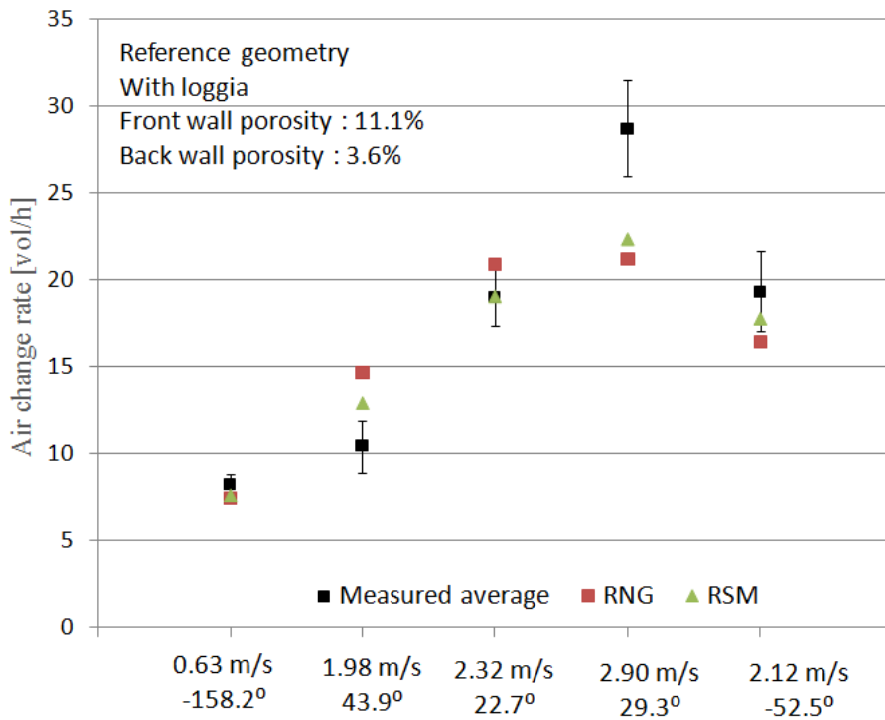


Figure 5. Comparison of ACH between experimental results and numerical simulations.

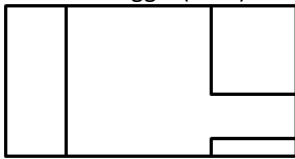
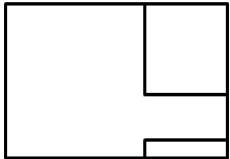
As for validation, the hill behind the building was modeled in the mesh. In the parametric analysis is in section 4, the hill is removed from the mesh to create an isolated environment.

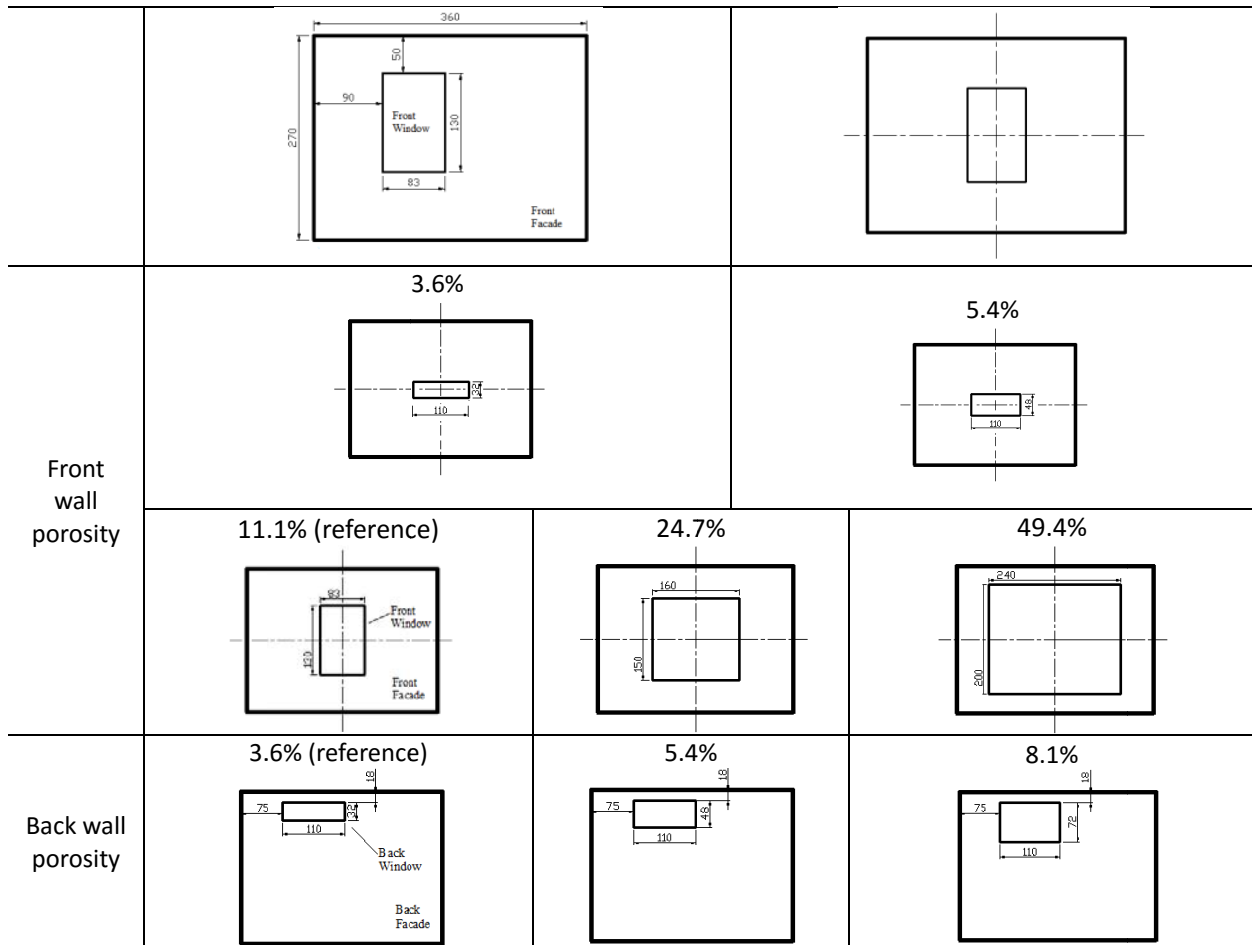
Figure 5 shows the ACHs determined simulation and experiments. Given the uncertainty of measurements, the ACHs from simulations are relatively reliable. The results of RSM are close to, even seemingly a bit more accurate than, those of RNG k-ε. However, RSM takes longer convergence time, so RNG k-ε is selected in the following analyses.

CFD Simulation about Impacts of Geometrical Parameters on Natural Ventilation

In the following parametric analysis, the geometry elements of the building envelope are varied. Each simulation is performed on a geometry that is a combination of the elements (Table 3).

Table3. Geometric changes in the cases of parametric analysis

Element	Configurations	
Loggia	<p>With loggia (CWL)</p> 	<p>Without loggia (CNL)</p> 
Position of front window	Reference (one-sided)	Centered



Impact of Loggia

Impact of Wind Incident Angle

The ACHs predicted by the correlation methods are much larger than the experimental results. This entails the necessity to investigate the impact of the loggia on the air flow. This part presents the simulations with Configuration with No Loggia (CNL) compared to the reference Configuration With Loggia (CWL) in the experiments. Except the loggia, the building geometry remained the same. In addition to the environment data obtained in the experiments, wind conditions were generalized for the parametric analysis.

The corresponding ACHs are shown in Fig.5. The wind velocity was set to be 2m/s and the wind incident angle, ϑ , varied from 0 to 180°.

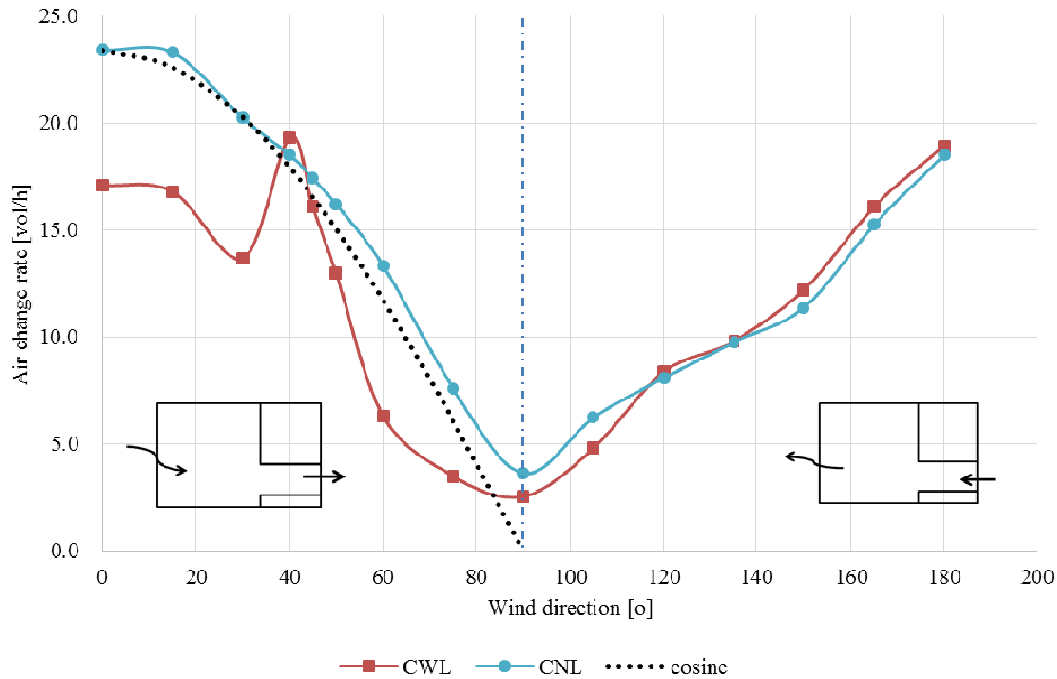


Figure 6. Air change rates in the function of wind incident angle, CWL and CNL, $v_{ref}=2\text{m/s}$.

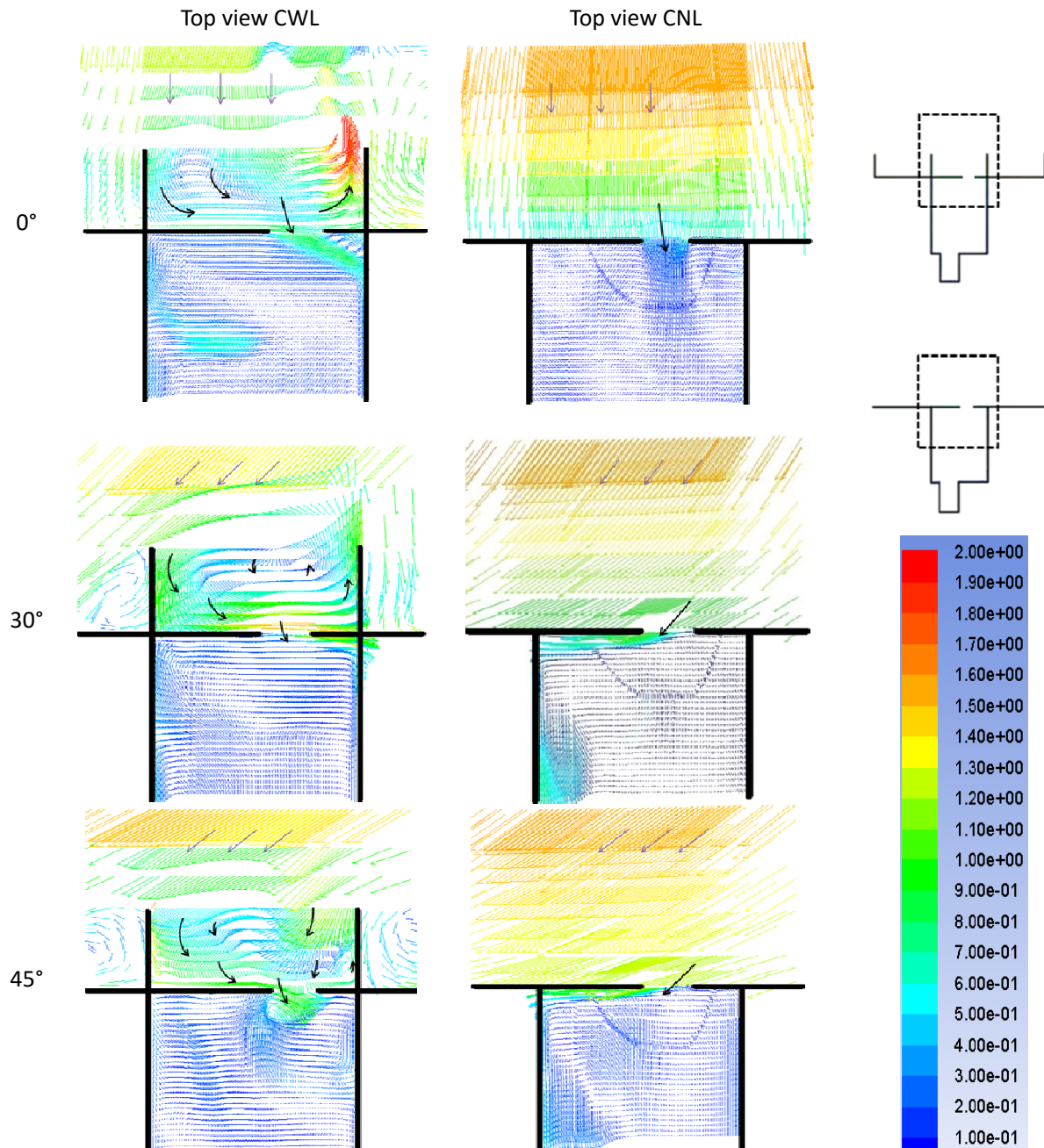
In case of CNL, the air change rate decreases when the wind incident angle ϑ increases, and the form is a cosine curve when ϑ is less than 75° . When ϑ approaches 90° , the ACH is minimized. The ACH will not be zero even when ϑ is 90° because the pressure fluctuation would create turbulence to induce airflow. The leeward part of the curves (right) is not the mirror of the windward part (left), despite the absence of the loggia. In the present configuration, the two windows on the front and back facades are not the same size, which leads to this dissymmetry.

In case of CWL, the ACH on the windward side is generally decelerated compared with CNL. On the windward side from $\vartheta=0$ to 90° , CWL reduces the ACH by 27% compared with CNL. A singularity exists, where the ventilation performance is improved, when ϑ is around 40° . The wind coming at the front window always ensures a larger ACH because of more significant turbulent flow on the larger opening. The CWL does not affect ACH if it is located at the outlet of the flow (leeward conditions).

A schematic explanation is presented to explain why the singularity at $\vartheta=40^\circ$ was not observed in the experiments, which depends on actual climate conditions in experiments. Figure 6 compares the velocity magnitude vector fields at the front wall opening among different wind incident angles. On a top view of the velocity field, it is clear that vortices are formed in the loggia area. This alters the wind direction and reduces the airflow velocity at the room opening, except in some cases. Between $\vartheta=30$ and 60° , with a climax at 45° , the loggia-induced vortex tends to direct the flow at the opening, limiting the reduction of the velocity component that is normal to the opening. At $\vartheta=45^\circ$, the velocity at the opening is 0.678 m/s , whereas it drops to 0.657 m/s at 30° and to 0.630 m/s at 60° . The presence of the vortex slows down the decrease of ventilation rate as long as ϑ is less than 60° . Once the wind direction exceeds this range, the side walls of the loggia truncate the wind inflow and the ACH drops dramatically.

As showed in Fig.6, the airflow approaching the building is weak at most tangential angles, but is reinforced at some others. At most tangential angles, ACHs are weakened by the vortex and some air

leaves the loggia without passing through the window. However, at ϑ around 40° , the airflow is mostly canalized by the loggia to flush indoor. The ACH increase under certain wind directions was not observed in the experiments because in real conditions, the wind fluctuation leads to continuous turbulence change inside the loggia, which can hardly form stable vortices as seen in the steady-state simulation.



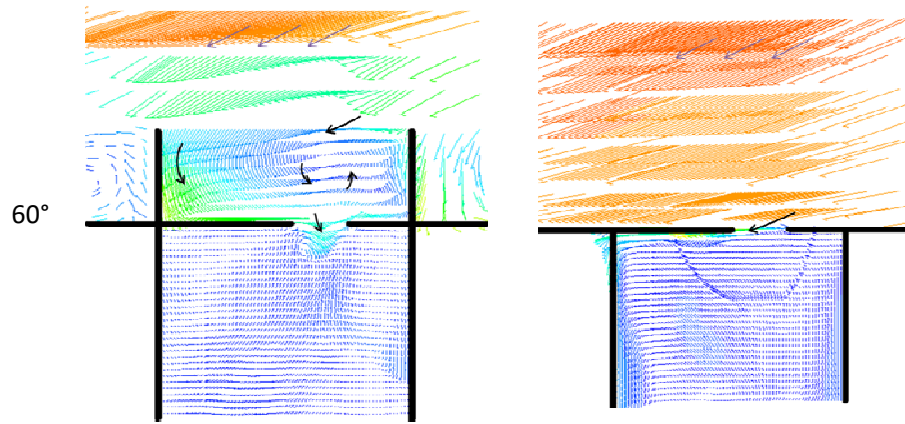


Figure 7. Wind velocity vector field at different wind incident angles, $v_{ref}=2\text{m/s}$, CWL and CNL. Top view on the mid-height of front window.

Impact of Opening Position

In the previous simulation, the front window was not positioned in the facade center, either horizontally or vertically. The window was installed 90 cm to the left wall and 50 cm to the roof. This corresponds to the original reference configuration and may be particular. To verify the generality of the loggia effect, we simulated the ACHs with the window positioned in the façade center (Fig. 7). The centered window was installed 1.4 m to both side walls and 70 cm to the roof. As showed in Fig. 8, the two ACH curves almost show the same shape, with a small phase difference of 5° . The two opening positions almost exert the same reduction effect on ACHs, which was not captured by the correlation methods. The singularity observed in the simulation is unidentifiable by in-situ experiments, since the wind is not steady.

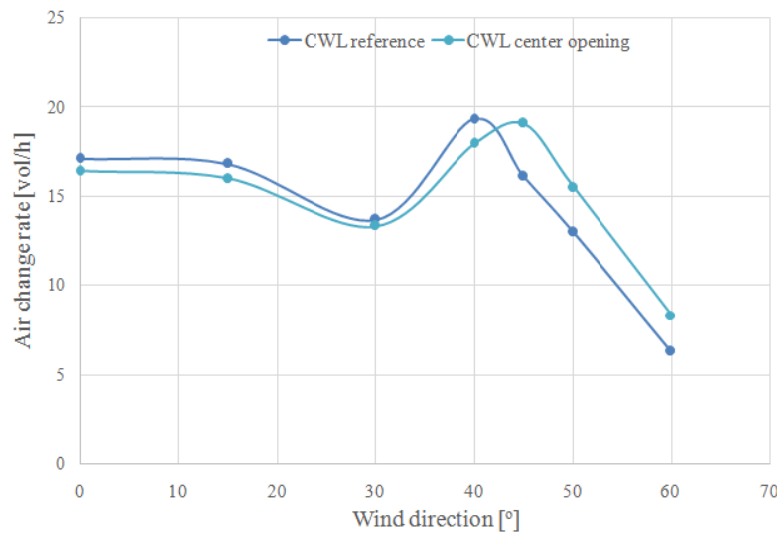


Figure 8. ACH for wind velocity $v_{ref}=2\text{ m/s}$, CWL reference and CWL with center opening.

Impact of Wind velocity

At larger wind velocities, the ACH curves relative to wind incident angle θ follow the same trend. As shown in Fig. 7, the ACHs generally decrease at larger ϑ . As showed in Fig.8, the ACHs at velocities of 4 and 6 m/s are 2.3 and 3.5 times larger than that at 2 m/s, respectively.

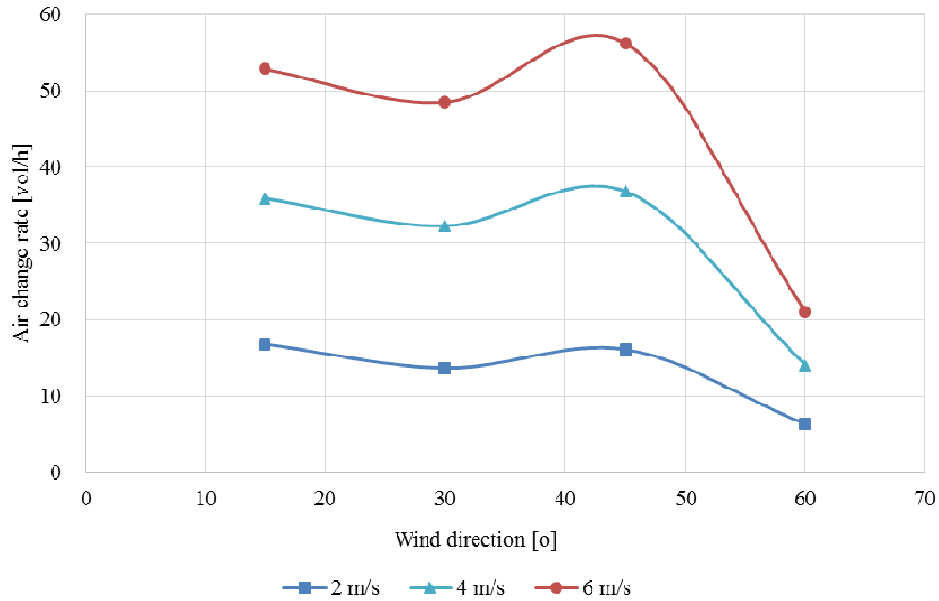


Figure 9. ACH at $v_{ref}=2, 4, 6$ m/s, CWL reference configuration.

Impact of Façade Porosity

As showed in Fig. 5, the simulation results are not symmetric between the windward side and leeward side even for CNL. None of the above mentioned correlation methods discriminate whether the wind arrives at the front wall or back wall. This phenomenon is attributed to the different sizes of the two openings. Specifically, the smaller opening surface became the major obstacle against airflow and therefore would control the ACH.

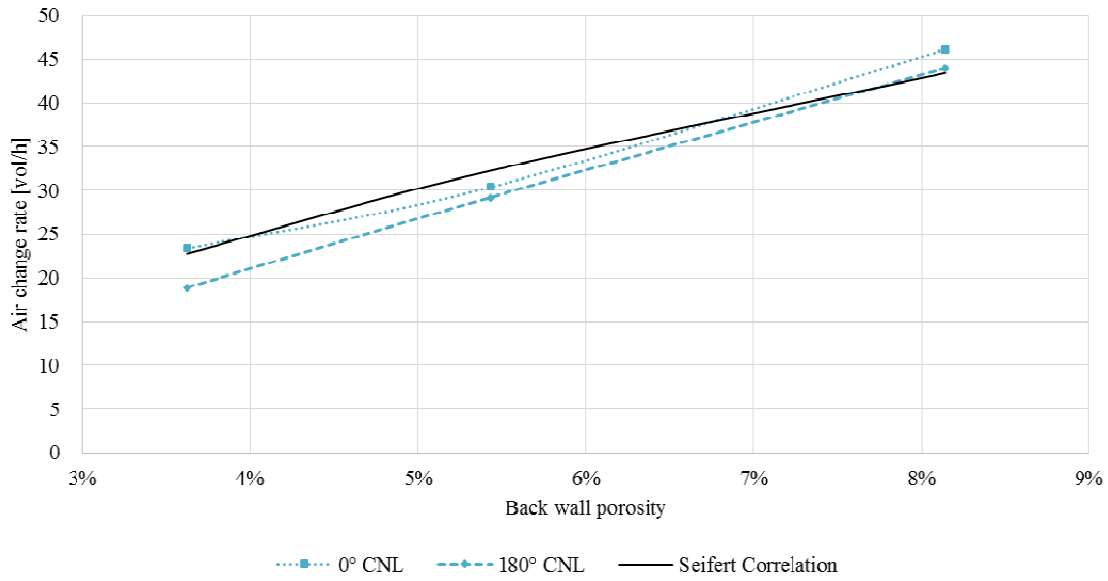
Equation (3) was generalized by Seifert et al. by introducing an effective opening surface when the openings, A_i , are not equal:

$$q = v_{ref} \cdot \sqrt{\frac{\Delta C_p}{\sum_i 1/(A_i^2 C_{d,i}^2)}} \quad (10)$$

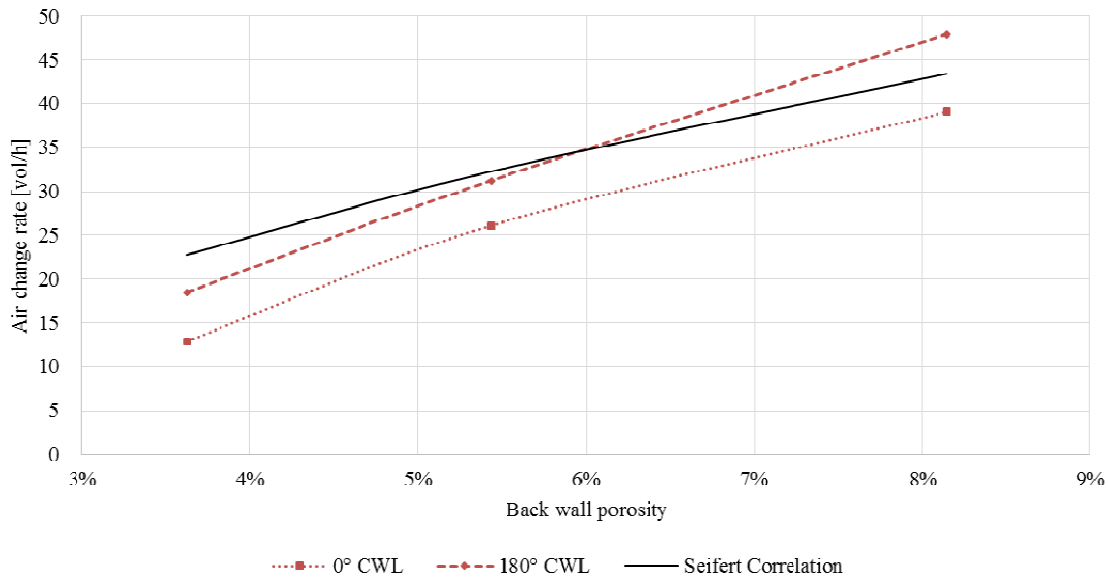
Where i represents the physical terms on each window opening. When the discharge coefficient C_d is constant, the airflow is controlled by the smaller openings and Eq. (10) predicts identical results between the windward and leeward sides.

To investigate the effects of opening size on ACH, we simulated with different opening sizes. The ACH varies when we successively change the opening size of back window (Fig. 10) and front window (Fig. 11).

As showed in Fig. 10, the geometry of the front window is fixed as in the reference configuration. The back window surface was enlarged by 1.5 and 2.25 times, which corresponds to porosity of 5.4% and 8.1% (limited by the room geometry). The wind speed was set to be 2m/s, and two wind directions ($0^\circ, 180^\circ$) were tested.



a) CNL

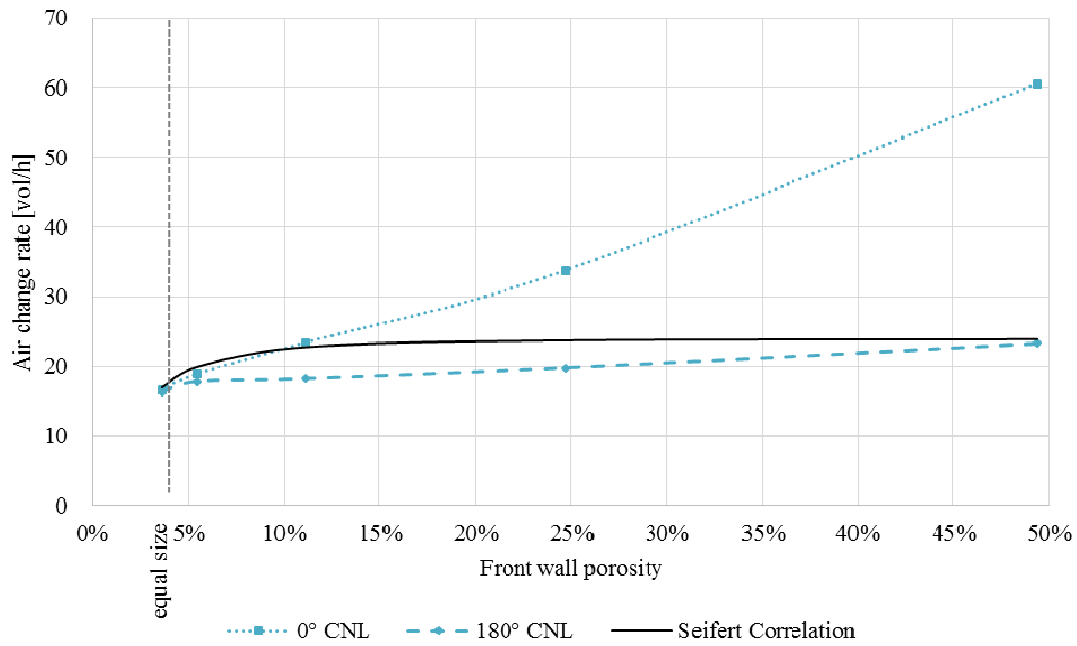


(b)CWL

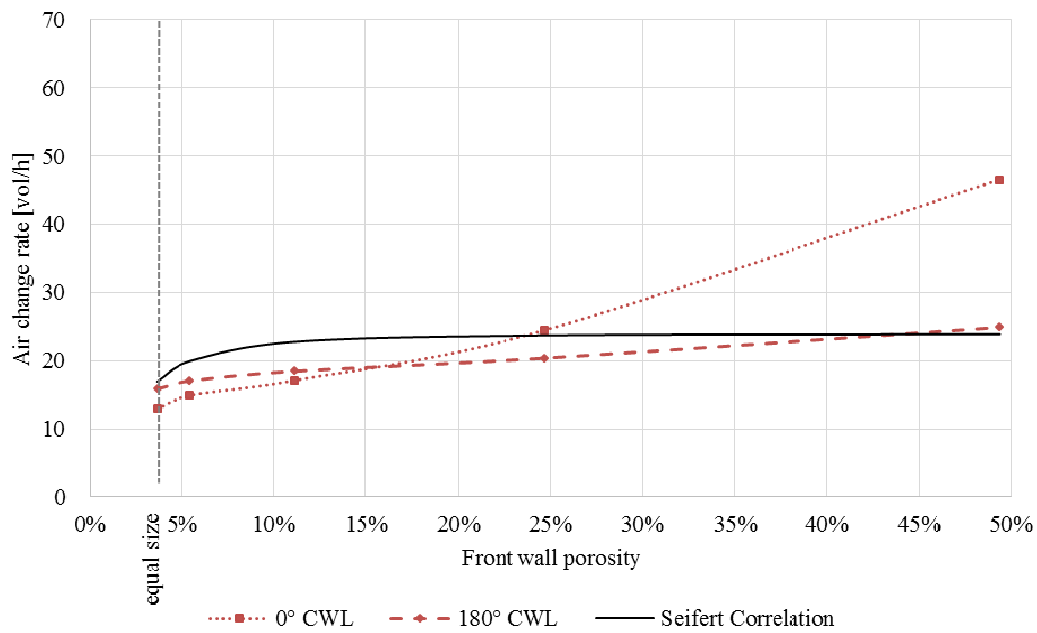
Figure 10. ACHs at varying back wall porosity (3.6%, 5.4% and 8.1%), $v_{ref}=2$ m/s, wind direction 0° and 180°, façade porosity = 11.1%.

When the back wall porosity is improved, the ACHs linearly increase as well because the openings are relatively small. Therefore, the Seifert correlation predicts the same trend as the numerical simulation. In the case of CNL, the correlation method yields positive results at both wind directions. In the case of CWL, the ACH under windward condition (0°) is reduced due to the 'loggia effect', while the ACHs under leeward condition (180°) are very close between CWL and CNL.

As showed in Fig.11, the back window geometry was fixed as in the reference configuration with a porosity of 3.6%. The front wall porosity was modified until it was 4 times the surface of the reference, with surfaces of 0.35, 0.53, 1.08, 2.4 and 4.8 m², corresponding to porosities of 3.6%, 5.4%, 11.1%, 24.7% and 49.4%, respectively. Two wind directions (0°, 180°) were tested.



a) CNL



b) CWL

Figure 11. ACHs at varying front wall porosity (3.6%, 5.4%, 11.1%, 24.7% and 49.4%), $v_{ref}=2$ m/s, wind direction 0° and 180° , back wall porosity = 3.6%.

It should be restated that the loggia reduces the ACH by around 30% underwindward condition (0°), but has no evident effect under leeward condition (180°), regardless of the front-wall porosity. Based on Fig. 10, we find:

- ACHs are quite close between windward and leeward conditions when the window sizes are equal for CNL.

- The CFD-predicted ACH increases slowly as the wall porosity increases under leeward condition.
- On the contrary, ACH significantly increases when the front opening size is enlarged under windward condition.
- Under windward condition, the results of the correlation diverge from those of the CFD. The ACHs from CFD simulations increase continuously for both CNL and CWL, whereas the ACH from the correlation method is limited by the smaller opening. The ACH difference between CFD and correlation method can be up to 146% when the opening ratio reaches 49.4% for CNL.

The failure of correlation methods in ACH calculation on large opening configurations has been reported. Using constant value of C_d is inappropriate for wind-induced ventilation that is characterized by pressure and velocity fluctuations [Chiu and Etheridge, 2007]. The correlation methods lose accuracy when two equally large openings are placed in the wind direction, because a dominant air stream is formed to largely reduce a building's airflow resistance [Shetabivash, 2015].

The present study confirms that the ACH calculation in the opening plan in wind-driven ventilation depends not only on the window size, but also on the wind direction. The correlation methods do not underestimate the ACH under leeward condition, even if the front window is quite large, and the deviation from CFD simulations remains under 30%. This indicates that the correlation methods can still be applied in a number of configurations when the window sizes on the opposite walls are not equal.

More-precise predictions require field measurements of C_d or CFD simulation. This is less convenient and more time-consuming than the use of correlation methods. The correlation methods tend to underestimate ACH for large openings under windward condition. The ACHs are high enough for large openings. The correlation methods are implanted according to the design guidelines and norms, so that it can be determined whether or not the design satisfies a minimum requirement of airflow rates.

Conclusions

We present a systematic evaluation of wind-driven natural ventilation performance in a low-rise hotel building configuration with loggia (CWL) or with no loggia (CNL) on the front façades. The simulation is based on 3D steady RANS CFD model.

The simulations show that CWL decreases ventilation performance under windward condition by 27%. Dominant wind from certain directions favors the cross-ventilation by forming a vortex in the loggia. In case of CNL, the simulation results are close to those of the correlations in all the leeward cases and in the windward cases where the opening sizes remain under 11% of the facade surface.

The correlation methods are adequate for the small facade porosity, but inadequate for large window sizes, especially under windward condition. Once the opening size is large enough, the ventilation rates increase significantly. This means larger window should be placed in the dominant wind direction rather than its opposite, in order to improve ventilation performance. It is also interesting in relating air change rate with the wind pressure in field measurements so as to better understand the ventilation mechanism for large facade porosity in future work.

For the design of ventilation performance, the actual correlation methods are accurate enough for low porosity. Under windward condition and for large porosity, C_d should be adjusted so as to use the correlation methods.

Acknowledgement

This work is funded by French National Research Agency under contract OVI-SOLVE. We appreciate that CEA INES and IESC provide the space for the experiments and ENTPE for the assistances in the experiments.

Nomenclature

q	Volumetric flow rate ($\text{m}^3 \cdot \text{s}^{-1}$)
C_0	Initial CO_2 concentration (ppm)
C_f	Final CO_2 concentration (ppm)
C_{bd}	Background CO_2 concentration (ppm)
C_d	Discharge coefficient (-)
A_{eff}	Effective flow area of the opening (m^2)
A_i	i -th opening (m^2)
C_p	Wind pressure coefficient (-) or Specific heat capacity at constant pressure ($\text{J} \cdot \text{kg}^{-1} \cdot \text{K}^{-1}$)
ACH	Air change rate, air changes per hour ($\text{vol} \cdot \text{h}^{-1}$)
V	test room volume (m^3)
S_{ct}	Turbulent Schmidt number (-)
T	Temperature (K)
T_0	Reference temperature (K)
u_i	i -th component of the velocity vector ($\text{m} \cdot \text{s}^{-1}$)
p	Precision (Pa)
v_{ref}	Reference wind velocity ($\text{m} \cdot \text{s}^{-1}$)
v_{wind}	Wind velocity ($\text{m} \cdot \text{s}^{-1}$)
\mathbf{v}	Velocity vector (u_1, u_2, u_3) ($\text{m} \cdot \text{s}^{-1}$)
Pr_t	Turbulent Prandtl number (-)
λ	Thermal conductivity ($\text{W} \cdot \text{m}^{-1} \cdot \text{K}^{-1}$)
k	Turbulent kinetic energy ($\text{m}^2 \cdot \text{s}^{-2}$)
ε	rate of dissipation of the turbulent kinetic energy
μ	Dynamic viscosity ($\text{kg} \cdot \text{m}^{-1} \cdot \text{s}^{-1}$)
μ_t	Turbulent viscosity ($\text{kg} \cdot \text{m}^{-1} \cdot \text{s}^{-1}$)
ρ	Density ($\text{kg} \cdot \text{m}^{-3}$)
θ	Wind incident angle ($^\circ$)
β	Thermal expansion coefficient (K^{-1})
g_j	j -th component of gravity vector ($\text{m} \cdot \text{s}^{-2}$)
HVAC	Heating, ventilation, and air conditioning
RANS	Reynolds-Averaged Navier Stokes equation modeling
RSM	Reynold Stress Model
RNG	Re-Normalisation Group k - ε Model
LES	Large Eddy Simulation
CWL	Cross-ventilation test With Loggia
CNL	Cross-ventilation test with No Loggia

